X-ray Absorption Spectroscopy Illustrates the Participation of Oxygen in the Electrochemical Cycling of $Li_4Mn_2O_5$

Haifeng Li[a,#], Indrani Roy[a,#], Mateusz Starczewski[a], John Freeland[b], Jordi Cabana[a,*]

[a]Department of Chemistry, University of Illinois at Chicago, Chicago, Illinois 60607, United States

[b]Advanced Photon Source, Argonne National Laboratory, Lemont, Illinois 60439, United States

[#]These authors contributed equally: Haifeng Li, Indrani Roy.

*Corresponding author: jcabana@uic.edu

Abstract

A combination of oxygen redox and Mn-based oxides would be the best option for high-energy density Li-ion batteries crucial for a sustainable society. The disordered rock-salt $Li_4Mn_2O_5$ was recently reported to display very large capacity of 460 mAh/g with relative reversibility. Previous studies proposed the involvement of lattice oxygen redox in such intriguing electrochemical performance, whereas no direct evidence was presented. To clarify the charge compensation mechanism, we systematically investigated the evolution of the electronic structure of both Mn and O upon cycling via Mn/O K-edge XAS spectroscopy. Mn K-edge XAS unequivocally demonstrates the participation of Mn redox upon the initial stages of charging, yet changes are arrested at the high potentials, while O continues to evolve according to O K-edge XAS. Upon discharging, both Mn and O partially recover to their pristine states. The results highlight the significance of a disordered structure in maintaining the reversible redox chemistry of both transition metals and oxygen to design cathode materials with high energy density.

1. Introduction

The call for a sustainable society powered by renewable energy from wind and solar imposes a significant demand for energy storage, particularly the wide deployment of Li-ion batteries with high energy densities.[1-3] Among the constituents in the battery, the cathode limits its storage capacity. Compared with conventional cathodes, Li-rich transition metal oxide cathodes ($Li_{1+x}TM_{1-x}O_2$, $0 < x < 1$, TM = transition metals) have gained attention in the battery field due to the transformational increase in the capacity arising from redox behavior that transcends classical cationic redox.[4-7]

So far, both Li-rich layered oxides with several 3d, 4d and 5d elements have been shown good electrochemical performance, such as $Li_{1.17}Ni_{0.21}Co_{0.08}Mn_{0.54}O_2$[8], Li_3RuO_4[9, 10], Li_2IrO_3[11, 12], Li_3IrO_4[10, 13], and Li_7RuO_6[14]. In terms of cost and sustainability, however, Mn-based Li-rich oxides are highly desirable, such as Li_2MnO_3[15-17] and $xLi_2MnO_3 \cdot (1-x)LiTMO_2$[5]. However, Layered Li_2MnO_3-based Li-rich oxides suffer from a deteriorative electrochemical cycling with voltage hysteresis and capacity decay due to the irreversible structural evolution,[8, 18-20] hampering their practical utilization. In order to bypass the detrimental structural degradation in Li-rich layered oxides, alternative materials with a disordered rock-salt (DRX) have been proposed.[21-25] These Mn-based DRX cathodes have shown promise in terms of energy density, impressive capacity retention and rate capability, the last of which is enabled by Li diffusion rate through percolating networks of TM-free clusters with low energy barriers.[26] Theoretically, there is no structural restriction in DRX materials compared with layered oxides which need to maintain their layered integrity upon electrochemical cycling. Thus, the horizon of chemical space in cathode design notably expanded.

Recently, a nanostructured disordered rock-salt-type $Li_4Mn_2O_5$ was developed, which displays an unusually high capacity of 460 mAh/g with relative reversibility.[27] Despite such intriguing electrochemical performance, the detailed charge compensation mechanism associated with (de)lithiation is still unclear. Based on measurements of magnetic properties, a previous study predicted that the electrochemistry of $Li_4Mn_2O_5$ was driven by cationic and anionic oxygen redox.[27, 28] Further studies in Mn K-edge X-ray absorption spectroscopy and Kβ X-ray emission spectroscopy uncover the partial oxidation of Mn^{3+} to Mn^{4+} and no existence of Mn^{4+}/Mn^{5+} redox couple, indicating that Mn redox activity can only partially account for the capacity observed,[29, 30] further hinting a significant involvement of oxygen upon the 1st cycling. While the same work suggested a very minor release of oxygen gas in the first cycle,[30] the evolution of electronic structure of oxygen after the same electrochemical processes has not directly been studied yet.

In pursuit of understanding the detailed charge compensation mechanism, in this work, X-ray absorption spectroscopy was performed at both Mn and O K-edges at various states of charge in the voltage window between 4.8 and 1.2 V. In combination with a quantitative analysis linking the oxidation state and absorption energy via integral method, Mn K-edge XAS clearly uncovered oxidation state changes of Mn in the initial stages of reaction. As a complementary probe to Mn K-edge XAS, O K-edge XAS unambiguously demonstrated changes of oxygen electronic structure upon cycling and uncovered that they dominate the charge compensation process at high voltage. The relatively reversible electrochemistry further verifies the significance of the disordered structure in sustaining the anionic oxygen redox.

2. Experimental section

2.1 Material Synthesis

$Li_4Mn_2O_5$ was synthesized via a two-step route, including a precursor preparation and mechanochemical activation, based on the previous reports. First, high-temperature $LiMnO_2$

precursor was produced via a traditional solid-state reaction by using a homogeneous reagent mixture of Li_2O (Sigma-Aldrich, 99.9%) and Mn_2O_3 (Sigma-Aldrich, 99.9%) under the stoichiometric ratio of 2:1. A small excess of (~5 wt%) of excess of Li_2O was added to compensate for the Li_2O loss at high temperature. Pellets weighing up to 1 g were pressed and calcined in a tube furnace at 1000°C under argon atmosphere for 12 h before cooling to room temperature (RT). The mechanical synthesis was carried out inside a stainless-steel jar with 8 stainless steel balls (10 nm in diameter) by using a Retsch PM200 Planetary Ball Mill at 600 rpm. The synthesized $LiMnO_2$ precursor was ballmilled with Li_2O with a stoichiometric molar ratio of 2:1 and carbon black (5 wt%) for 24 h.

2.2 Characterization

2.2.1 Electrochemical Testing

All electrochemical characterizations of galvanostatic charge–discharge experiments were performed in two-electrode 2032 coin-type cells. The positive electrode materials were homogeneously mixed in a planetary ball mill in argon-filled glovebox with 10 wt% carbon black (Denka) under Argon atmosphere before further experiments. The mixture powder was then used as cathode materials for the coin cell assembling. The cells were fabricated in an argon-filled glovebox with moisture and oxygen levels of lower than 0.1 ppm. Within the cells, a high-purity lithium foil (Alfa Aesar) was employed as the counter/reference electrode, and a Whatman GF/D borosilicate glass fiber was employed as separator, and a solution of 1 M LiPF6 dissolving in a mixture of ethylene carbonate (EC)/dimethyl carbonate (DMC) (1:1, V/V, Novolyte Technologies) was employed as the electrolyte. During the experiment, the typical loading of powdered active material was 10 mg in a typical cell. The galvanostatic charge–discharge cycling with the voltage window of 4.8 - 1.2 V was performed at RT using a BT-Lab tester with a current rate of C/10 (indicating 1 Li is extracted in 10 h) with variant voltage-cutoff windows. All potentials quoted in this paper were referenced to Li^+/Li^0 unless otherwise mentioned. When the state of the charge reaches the setup point, the cell would be immediately disassembled in the argon-filled glovebox to avoid self-discharging under open-circuit state and the inside cycled electrode powder was washed thoroughly with anhydrous DMC and then dried under vacuum via the glovebox antechamber for 5 mins. Cleanly dried electrodes would be stored in the argon-filled glovebox for the future *ex situ* characterization.

2.2.2 Structural Characterization

The lab XRD was collected by using Bruker D8 Advance under Cu Kα radiation with the wavelength of 1.5406 Å. *Ex situ* high resolution synchrotron X-ray diffraction (SXRD) measurements were conducted at the 11-BM-B beamline at the Advanced Photon Source (APS) at Argonne National Laboratory (ANL) via a 12-channel analyzer detector array, with an average wavelength of 0.412795 Å produced by two platinum-striped collimating mirrors and a double-crystal Si(111) monochromator. The data was collected with a step size of 0.001° (2θ) and a scan speed of 0.01°/s. The powder samples were mixed with an appropriate amount of amorphous silicon dioxide to reduce X-ray absorption. Air-sensitive samples for *ex situ* measurements were sealed in Kapton capillaries with a diameter of 0.80 mm in an Ar-filled glovebox, and subsequently packed into heat-sealed Al-coated plastic bags for transport to the instrument. The capillaries were transferred out of the bag right before their measurement to minimize their exposure to air to the time required for the measurement. Time of flight neutron powder diffraction (TOF-NPD) data were collected at room temperature at the beamline 11A (POWGEN) of the Spallation Neutron Source (SNS) at Oak Ridge National Laboratory (ORNL) with the center wavelength of neutrons of 1.5 Å. An appropriate amount of sample was sealed in airtight vanadium sample cans with an inner diameter of 6 mm under argon and transferred to the beamline station. Rietveld Refinements were performed through the GSASII program.[31]

2.2.3 X-ray Absorption Spectroscopy

Ex situ **Mn L-edge and** O K-edge X-ray absorption spectroscopy (XAS) was collected at the 4-ID-C beamline at the APS. Data were obtained at a spectral resolution of ~0.2 eV, under both total fluorescence yield (TFY) and total electron yield (TEY) modes. Harvested samples were stored in an Ar-filled glovebox, transferred into a portable transport container and then into the instrument antechamber under an Ar environment to minimize the potential exposure to air. During the measurement, three scans were performed on each sample, at each absorption edge, and scans were averaged to maximize the signal-to-noise ratio. The O K-edge XAS was calibrated to a Sr_2RuO_4 reference measured simultaneously with the sample, while the Mn L-edge was calibrated to a Mn reference measured simultaneously with the sample.

Ex situ Mn K-edge XAS was collected at the 20-BM-B beamline at the APS in transmission mode using a Si (111) double crystal monochromator. A standard foil of Ru metal located in front of a reference ion-chamber for Mn K-edge was measured simultaneously with each spectral sample for energy calibration. The energy threshold E_0 of the reference Mn foil was determined from the first derivative peak of the spectrum, and all XAS reference spectra were calibrated and aligned to the standard Mn energy for further comparison study. The background subtraction, X-ray absorption near edge spectroscopy (XANES) normalization and (extended X-ray absorption fine structure (EXAFS) fitting were carried out using IFEFFIT-based Demeter package.[32]

3. Results and discussion

3.1 Electrochemical properties

The X-ray diffraction patterns of the as-synthesized sample agrees well with the previous report[27] (Figure S1), verifying the consistency in the crystal structure of the sample. Upon initial oxidation, the electrochemical profile showed a pseudo plateau, with the onset from 3.3 V and end at 3.5 V, followed by a sloping profile to 4.8 V, amounting to a specific capacity around 473 mAh/g, equivalent to the removal of 4 mol of Li per mol of compound, assuming 100% faradaic efficiency (Figure 1a). The corresponding derivative, dQ/dV, depicted a sharp peak centered at 3.4 V and a small one at 4.18 V (Figure 1b). Upon the subsequent reduction, the profile displayed no observable plateaus. There was a broad peak at 2.95 V, with a shoulder around 3.3 V, and a comparably smaller one at 1.58 V in dQ/dV. It is noted that not all the Li extracted in the first oxidation was re-inserted into the compound, in agreement with previous reports[27] and also reflects the irreversibility in the electrochemical response. The profiles starting from the 2nd cycle are significantly different compared with that of the 1st (de)lithiation. The anodic steps started at 3.1 and 4.12 V, respectively, while the cathodic processes shifted to 2.9 V, with a dramatic decrease in peak width, and to 1.68 V, with a prominent decrease in the intensity, reflecting a noticeable decrease in the voltage hysteresis compared with that of the 1st cycle. In addition, a new process emerged at 4.0 V. Upon subsequent cycling, the profiles largely remained steady, with a minor evolution in the shape and a decrease in hysteresis, reflecting highly reversible (de)intercalation processes. Generally, the electrochemical behavior of the as-synthesized material is analogous to the previous reported one.[27, 29] In addition, the comparison between the 1st cycling and subsequent cycling indicates the material underwent an activation during the 1st charge-discharge process, which will be the focus of the following discussion. It has previously been proposed that the as-made material contains a small amount of unreacted Li_2O, which then participates in the 1st charge,[29] in an irreversible process. Since $Li_4Mn_2O_5$ was prepared via the same method as reported[27], the existence of Li_2O can also explain the difference of the electrochemical behavior between the 1st cycle and the subsequent cycles observed here. In terms of the potential oxygen loss upon cycling, Diaz-Lopez studied the gas evolution via *in situ* online electrochemical mass spectroscopy (OLMS) and revealed that there is only tiny oxygen gas release.[30] Therefore, this trace oxygen loss have little effect on the irreversible electrochemical performance.

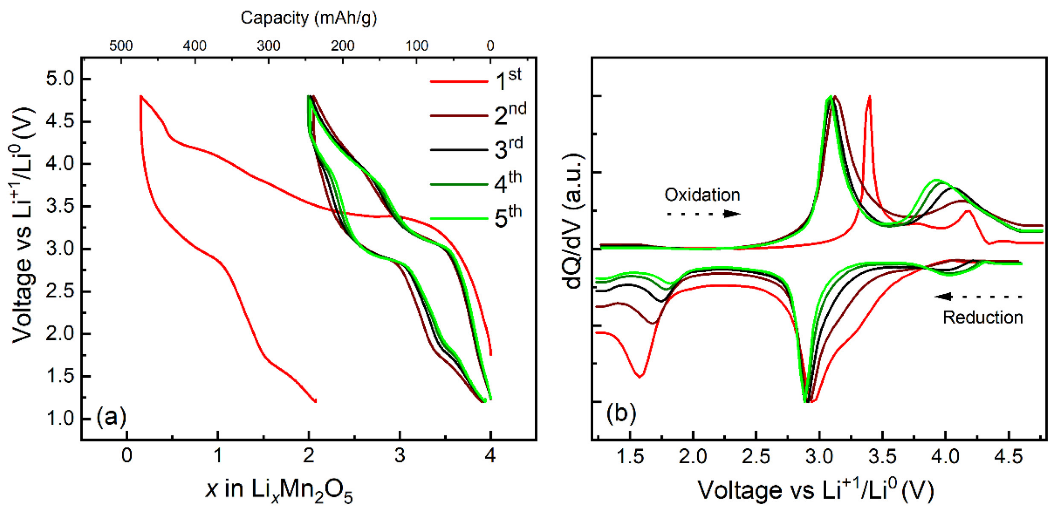

Figure 1. (a) Voltage-composition profiles of $Li_4Mn_2O_5$ during the first five charge-discharge processes in the voltage window of 1.5-4.8 V and (b) the corresponding differential capacity plots.

3.2 *Ex* situ Mn K-edge XAS

To gain a full understanding of the role of Mn in the charge compensation upon cycling, *ex situ* Mn K-edge XAS were performed at various states of charge (Figure 2a). The Mn K-edge XAS can be divided into two regions, a small pre-edge around 6542 eV and an absorption edge above 6545 eV. The main absorption edge arises from the electric dipole-allowed transition from 1s to 4p level, while the pre-edge originates from two primary transitions[33]. One is the electric quadrupole-allowed and dipole-forbidden 1s → 3d transition. The probability of the electric quadrupole-allowed transitions is much lower compared with the dipole transition, leading to a much lower intensity in the pre-edge peak unless the coordination environment is non-centro-symmetric, due to the mixing between 3d and 4p orbitals. The shape of the Mn K-edge XAS spectra underwent a notable evolution with cycling, which is confirmed by the spreading out of the 1st derivative plots (Figure S2). This phenomenon introduced uncertainty in the determination of the oxidation state of Mn by simple methods such as comparing the absorption edge or 1st derivative plots. In view of this uncertainty, the integral method reported by Dau et al. was employed (Figures 2b and 2c),[34] rather than analyses based on single points, to maximize accuracy and probe uncertainty in establishing the relationship between the position of the absorption edge and the nominal oxidation state.

The absorption edge of the pristine $Li_4Mn_2O_5$ is located at slightly lower energy than $Mn_2^{3+}O_3$ (Figure 2a), suggesting that it may contain small amounts of Mn^{2+} in addition to Mn^{3+}. The spectrum also has a weak doublet pre-edge feature at 6540.5 and 6542.7 eV (Figure 2b), corresponding to quadrupole electric transition to t_{2g} and e_g orbitals. Upon oxidation to 3.7 V, coulometry indicates that approximately 1 mol electrons were extracted from $Li_4Mn_2O_5$ (Figure 1a), assuming 100% faradaic efficiency. In turn, the absorption edge largely shifted to higher energy than $Mn_2(III)O_3$, reflecting the oxidation of Mn. The exact change in oxidation state was sensitive to the choice of endpoints in the integration (Figures 2c and 2d and Figure S3 and associated discussion), going from 2.7-2.8 in the pristine state to 3.4-3.5 at 3.7 V. The extent of change at the Mn K-edge, equivalent to 0.7-0.8 electrons per Mn, was comparable to previous reports[30] and in reasonable agreement with coulometry, especially considering that our analysis highlights the sensitivity of the quantification to analytical choices. The pre-edge experienced an increased intensity with a well-resolved doublet due to a further distortion of the Mn coordination environment to more non-centrosymmetric one driven by delithiation, consistent with Mn oxidation process based on that the intensity of the pre-edge feature is inversely related to the number of 3d electrons.[33] Upon further oxidation, the peak of the white line, at ~6561.4 eV, shifted to higher energy and the intensity of the pre-edge feature increased further, yet the absorption edge largely stayed static (Figures 2a and 2b), indicative of a preservation of Mn oxidation state which is reflected in the analysis via integration (Figures 2c and 2d). The change in Mn oxidation state cannot solely account for the large, delivered capacity, equivalent to ~0.9 mol electrons per mol Mn. Upon the reversal of the current to reduce to 2.4 V, the lithiation process gave rise to a low energy shift, to an average oxidation state of 3.0, and a reduction in the pre-edge peak intensity. Further reduction to 1.2 V recovered the spectrum to the pristine state in both the absorption edge and pre-edge region (Figures 2a and 2b), with a final Mn oxidation state of 2.7, indicating a relative reversibility in Mn redox state during the 1st cycle.

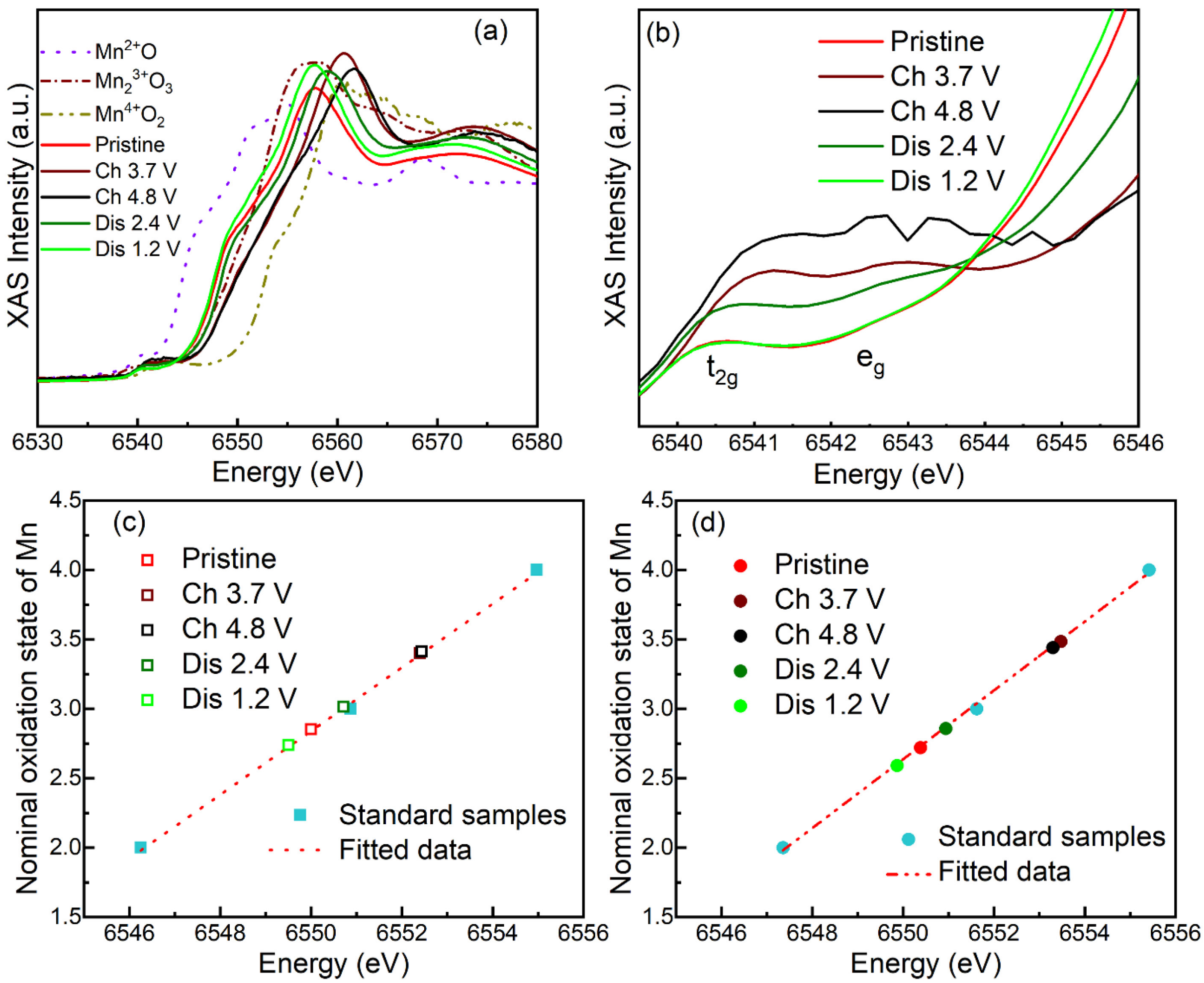

Figure 2. (a) Mn K-edge XANES of $Li_4Mn_2O_5$ at different states of charge, compared with the reference samples: $Mn^{2+}O$, $Mn_2^{3+}O_3$, and $Mn^{4+}O_2$. (b) Mn pre-edge features at different states of charge of $Li_4Mn_2O_5$ during the first cycle. (c) and (d) Relationship between the absorption edge energy and nominal oxidation state of Mn in the spectra (a). The integrated regions for integrating are between 0.2 and 0.8 in the values of intensity for (c) and between 0.3 and 0.7 for (d). The detailed oxidation states of Mn and parameters of the fitted data are shown in Table S1.

3.3 *Ex* situ Mn L-edge XAS

Although Mn K-edge XAS spectra provide the evolution of the average oxidation state of Mn in the bulk, the variation of the electronic structure of Mn on surface is missing. Hence, Mn L-edge XAS, arising from transitions from Mn 2p states to unfilled Mn 3d orbitals, were collected under TEY mode with a penetration of 10 nm to probe chemical states of Mn on the surface (Figure 3). Due to the broad feature in L_2 region, the comparably resolved peaks in the L_3 region are the focus. In comparison with reference samples,[35] the pristine spectrum demonstrated the existence of peak a and peaks c and d corresponding to Mn^{2+} and Mn^{3+}, respectively, revealing that Mn in the pristine $Li_4Mn_2O_5$ on the surface is the mixture of Mn^{2+} and Mn^{3+}, consistent with the average oxidation state of Mn lower than 3+ in the bulk deduced from Mn K-edge XAS. Upon oxidation to 3.7 V, the intensity of peaks c and d, and peaks b and e, corresponding to Mn^{3+} and Mn^{4+}, respectively, increased and the intensity ratio between peak a and other peaks decreased, indicating the oxidation of Mn associated with delithiation and the mixed state of Mn^{2+}, Mn^{3+} and Mn^{4+}. Further oxidation to 4.8 V reduced the intensities of peaks c and d and largely increased the intensity of peak e, suggesting the increase in Mn^{4+} at the expense of Mn^{3+}. However, it is important to note that the average oxidation state at the surface was decidedly lower than in the bulk, probed by Mn K-edge XAS. This discrepancy points at a possible involvement of interfacial reactions to faradaic inefficiencies of the electrode during charge.

Reduction to 2.4 V noticeably decreased the intensities of peak b and e and increased peak d, uncovering the reduced amount of Mn^{4+} and increased Mn^{3+}. Subsequent reduction to 1.2 V resulted in a vanished peak b, reflecting the absence of Mn^{4+}, and increased the intensity ratio of peak a to other peaks, indicating the increased amount of Mn^{2+} and, thus, a final mixed state of Mn^{2+} and Mn^{3+}. In comparison with the pristine state, the spectrum after reduction to 1.2 V was not fully recovered, indicating the partial reversibility of the redox process.

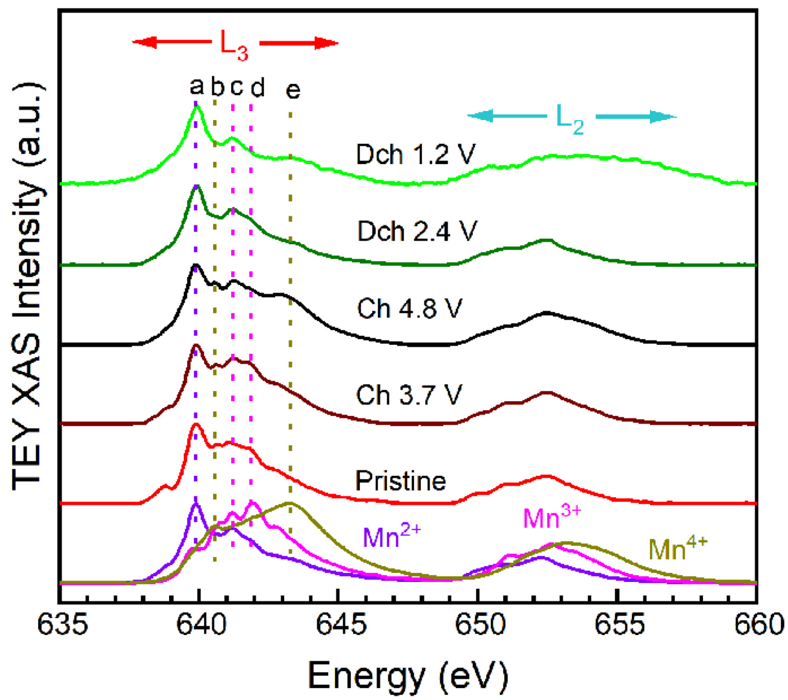

Figure 3. *Ex situ* Mn L-edge XAS spectra of $Li_4Mn_2O_5$ at different states of charge measured under TEY mode. Mn L-edge XAS spectra of reference samples $Mn^{2+}O$, $Mn_2^{3+}O_3$ and $Mn^{4+}O_2$ collected at the same mode are provided for comparison.

3.4 *Ex situ* O K-edge XAS

Although Freire et al.[27] and Diaz-Lopez et al.[30] proposed that lattice O redox plays an important role in the extra capacity of $Li_4Mn_2O_5$, no experimental evidence was provided to support the participation of O in the charge compensation. Therefore, we performed the O K-edge XAS analysis of $Li_4Mn_2O_5$ at various charged and discharged states. The O K-edge XAS probes dipole allowed transition from core O 1s to empty O 2p states.[36] In general, the spectrum of O K-edge XAS can be divided into two regions (Figure 4). The pre-edge (< 535 eV) represents the unoccupied states resulting from O 2p orbitals hybridized with TM 3d orbitals, and the broad band above 533 eV corresponds to a collection of excitations from O 1s to orbital to empty states of O

2p orbitals mixed with the TM 4s and 4p orbitals, and ultimately, the continuum. The position of the pre-edge peak is affected by the change in the net electron density of the ligand via donating charge to the surrounding metal ion, the degree of d orbital splitting induced by the ligand field effect, and the overall TM d-manifold orbital energy determined by the strength of the covalent TM-O bonds.[37] The intensity of these peaks reflects both the density of unoccupied hybridized states and the contribution of O to their wave function. Therefore, the measurements offer insight into the role of O states and any changes in covalency.[38] Note that the XAS spectra were measured simultaneously under both TEY and TFY modes. The TEY mode with a probing depth around 10 nm provides surface information, whereas the TFY mode probes 100 nm into the electrode, offering insight into the interior of the material. It is worthy of notice that the spectral intensities in this mode are distorted due to the self-absorption phenomenon of fluorescent photons by the material, so only qualitative trends between samples will be discussed.

In terms of O K-edge XAS collected at TFY mode, the O K-edge XAS of the pristine state displayed two broad features located at ~531.0, ~532.4 eV, respectively (Figures 4a and S4a), which is due to the transition to unoccupied O 2p states hybridized with Mn 3d states based on the previous studies.[39, 40] Apart from that, a broad peak centered ~533.9 eV was above the background. Freire et al. confirmed the existence of the residue Li_2O in the bulk during the synthesis of $Li_4Mn_2O_5$ by employing neutron and synchrotron diffraction.[29] Previous O K-edge measurements of Li_2O[41] revealed a broad pre-edge feature at ~533.9 eV, suggesting the existence of Li_2O in the bulk of our samples, as well, even if it was undetected by laboratory XRD. It is worth noting that Li_2CO_3 has a sharp feature at similar energies,[41] so, given the high background at these energies, the possibility of the carbonate contributing to the signals cannot be excluded with high confidence.

The oxidation to 3.7 V largely reconstructed the spectral shape and led to well-resolved peaks at 529.6 and 532.0 eV with a large increase in peak intensities, assigned to the transition to t_{2g} and e_g states in Mn^{4+},[18 42] consistent with the Mn K-edge data. Further oxidation continued to increase peak intensities without altering peak positions, reflecting the continual increase of unoccupied O 2p states. Since there was no Mn oxidation during this process and little oxygen gas loss was observed[30], the displayed large capacity is ascribed to involvement of O in the oxide lattice in the charge compensation. The notable decrease in relative intensity at 533.9 eV would also be consistent with the oxidation of Li_2O to O_2 during charging, as proposed in the literature.[43] Reduction to 2.4 V resulted in a significant change in the spectral shape with a broad peak centered at 531.8 eV and two shoulders at 531.0 and 529.9 eV and a pronounced decrease in the intensity due to the decreased O-Mn covalency mainly derived from the Mn reduction, consistent with Mn K-edge XAS. Further reduction to 1.2 V largely preserved the overall spectral shape of the pre-edge, but led to a decrease in its intensity, further supporting the Mn reduction involving the electrons filling O 2p-Mn 3d covalent states. It is noticeable that the TFY spectra did not fully recover to the pristine state during discharge, indicating that the changes in the O electronic structure in the bulk are not completely reversible. Some of the irreversibility is ascribed to the contribution of Li_2O oxidation to the capacity on charge,[29] since there was no recovery of the signals at 534 eV. The fact that the pre-edge at 1.2 V had notably lower total intensity than the pristine sample would suggest that the compound was reduced beyond its initial state at these potentials.

The TEY O K-edge XAS spectrum of pristine $Li_4Mn_2O_5$ exhibited a broad pre-edge feature below 535 eV (Figures 4b and S4b). There was a sharp peak located at ~533.6 eV. This peak appeared to be meaningfully redshifted compared to the broad peak centered at 533.9 eV observed in TFY of the pristine state. The energy and lineshape differences are reminiscent of the reported differences between the O K-edge XAS of Li_2CO_3 and Li_2O.[40] Therefore, while again a contribution of Li_2O cannot be completely discarded, the sharp peak appears to be dominated by the transition to π* (C = O) orbital of Li_2CO_3 existing mainly on the surface[41, 44] There were two shoulder features located at the same positions as those in the bulk, that is 531.0 and 532.4 eV, respectively, but with a much lower intensity mainly due to the small amount of the active material on the surface. Oxidation to 3.7 V maintained the 531.0-eV peak and shifted 532.4-eV peak to left by 0.4 eV and brought about a large intensity increase, indicating an increased empty O 2p-Mn 3d hybridized states, and generated a new peak at ~529.6 eV, which are due to the oxidation of partial Mn on the surface from Mn L-edge XAS spectrum. Upon further oxidation, the peak at 531.0 eV was preserved with a small intensity increase, and the previous peak at 532.0 eV experienced a right shift by 0.2 eV and a slight decrease in the intensity. This oxidation process led to a significant enhancement in the intensity of 529.6 eV peak without variation in position, indicative of large increase in unoccupied O 2p-Mn 3d hybridized states due to Mn oxidation on the surface. As in the Mn L-edge data, there was a clear discrepancy in the degree of oxidation of the surface and the bulk at the same charging potential, pointing at detrimental interfacial processes contributing unproductive capacity during charge.

The reverse reduction decreased 531.0-eV peak intensity and shifted the previous 531.8-eV peak to 532.0 eV with a slight increase in intensity and resulted in the vanishment of the 529.6-eV peak due to the electron filling of O^{2-} from Mn reduction. Further reduction to 1.2 V continuously gave rise to a significant decline in 531.0-eV peak and almost remained the position of 532.0-eV peak yet with a decrease in the intensity. Analogous with TFY spectrum, the spectrum did not completely recover to the pristine state, again reflecting the partial reversibility of O electronic structure on the surface. The complicated evolution of O K-edge XAS is also consistent with the mixed chemical states of Mn on the surface and the irreversible involvement of Li_2O.

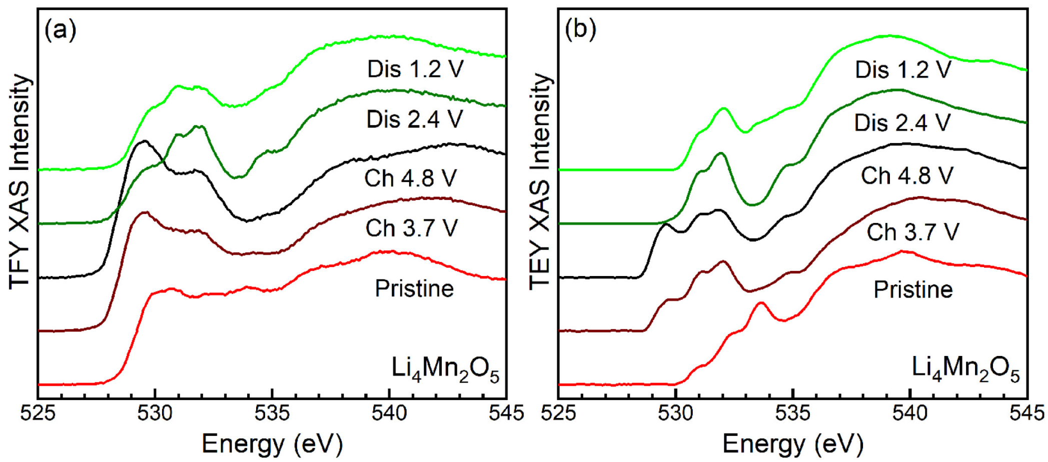

Figure 4. Stacked *ex situ* O K-edge XAS spectra of $Li_4Mn_2O_5$ at different states of charge measured under TFY (a) and TEY (b) mode.

4. Conclusion

In summary, we performed a combination analysis of Mn K-edge XAS and O K-edge XAS at different states of charge of $Li_4Mn_2O_5$ with a disordered rock-salt structure. The combination of a qualitative study and quantitative analysis of Mn K-edge XAS spectra clearly unraveled the involvement of Mn redox with formal changes in oxidation state that only matched the measured capacities up to 3.7 V, at best, remaining steady at higher potential. Complementary O K-edge XAS unambiguously demonstrated changes of oxygen electronic structure at all stages upon cycling, even when Mn did not change at high potential. Thus, the results uncovered the dominant contribution of oxygen to the charge compensation required to achieve the highest levels of delithiation. Further studied are needed to elucidate reversible and irreversible aspects of this reactivity, such as lattice stability and interfacial release of O species, especially in view of the irreversible changes undergone by the electronic structure of the material. The relatively reversible evolvement of O/Mn electronic structure further verifies the significance of the disordered structure in sustaining reversible redox.

ASSOCIATED CONTENT

Supporting Information

The Supporting Information is available free of charge.

XRD data of the pristine $Li_4Mn_2O_5$, derivative analysis of Mn K-edge XAS, integral analysis, overlaid O K-edge XAS, Table S1 describing linear fitting parameters of Mn K-edge XAS analysis.

Acknowledgements

This material is based upon work supported by the National Science Foundation under Grant No. DMR-1809372. This research used resources of the Advanced Photon Source, a U.S. Department of Energy (DOE) Office of Science User Facility operated for the DOE Office of Science by Argonne National Laboratory under Contract No. DE-AC02-06CH11357. Neutron diffraction data were collected at the POWGEN beamline at the Spallation Neutron Source, Oak Ridge National Laboratory, which was sponsored by the Scientific User Facilities Division, Office of Basic Sciences, U. S. Department of Energy.

References

(1) Zubi, G.; Dufo-López, R.; Carvalho, M.; Pasaoglu, G. The lithium-ion battery: State of the art and future perspectives. *Renewable and Sustainable Energy Reviews* **2018**, *89*, 292-308. DOI: https://doi.org/10.1016/j.rser.2018.03.002.
(2) Trahey, L.; Brushett, F. R.; Balsara, N. P.; Ceder, G.; Cheng, L.; Chiang, Y.-M.; Hahn, N. T.; Ingram, B. J.; Minteer, S. D.; Moore, J. S.; et al. Energy storage emerging: A perspective from the Joint Center for

Energy Storage Research. *Proceedings of the National Academy of Sciences* **2020**, *117* (23), 12550-12557. DOI: 10.1073/pnas.1821672117.
(3) Chen, T.; Jin, Y.; Lv, H.; Yang, A.; Liu, M.; Chen, B.; Xie, Y.; Chen, Q. Applications of Lithium-Ion Batteries in Grid-Scale Energy Storage Systems. *Transactions of Tianjin University* **2020**, *26* (3), 208-217. DOI: 10.1007/s12209-020-00236-w.
(4) Rozier, P.; Tarascon, J. M. Review—Li-Rich Layered Oxide Cathodes for Next-Generation Li-Ion Batteries: Chances and Challenges. *Journal of The Electrochemical Society* **2015**, *162* (14), A2490-A2499. DOI: 10.1149/2.0111514jes.
(5) Thackeray, M. M.; Kang, S.-H.; Johnson, C. S.; Vaughey, J. T.; Benedek, R.; Hackney, S. A. Li2MnO3-stabilized LiMO2 (M = Mn, Ni, Co) electrodes for lithium-ion batteries. *Journal of Materials Chemistry* **2007**, *17* (30), 3112. DOI: 10.1039/b702425h.
(6) Sathiya, M.; Rousse, G.; Ramesha, K.; Laisa, C. P.; Vezin, H.; Sougrati, M. T.; Doublet, M. L.; Foix, D.; Gonbeau, D.; Walker, W.; et al. Reversible anionic redox chemistry in high-capacity layered-oxide electrodes. *Nature materials* **2013**, *12* (9), 827-835. DOI: 10.1038/nmat3699.
(7) He, W.; Guo, W.; Wu, H.; Lin, L.; Liu, Q.; Han, X.; Xie, Q.; Liu, P.; Zheng, H.; Wang, L.; et al. Challenges and Recent Advances in High Capacity Li-Rich Cathode Materials for High Energy Density Lithium-Ion Batteries. *Advanced Materials* **2021**, *33* (50), 2005937. DOI: https://doi.org/10.1002/adma.202005937.
(8) Gent, W. E.; Lim, K.; Liang, Y.; Li, Q.; Barnes, T.; Ahn, S. J.; Stone, K. H.; McIntire, M.; Hong, J.; Song, J. H.; et al. Coupling between oxygen redox and cation migration explains unusual electrochemistry in lithium-rich layered oxides. *Nature communications* **2017**, *8* (1), 2091. DOI: 10.1038/s41467-017-02041-x.
(9) Jacquet, Q.; Perez, A.; Batuk, D.; Van Tendeloo, G.; Rousse, G.; Tarascon, J.-M. The Li3RuyNb1 − yO4 (0 ≤ y ≤ 1) System: Structural Diversity and Li Insertion and Extraction Capabilities. *Chemistry of Materials* **2017**, *29* (12), 5331-5343. DOI: 10.1021/acs.chemmater.7b01511.
(10) Li, H.; Ramakrishnan, S.; Freeland, J. W.; McCloskey, B. D.; Cabana, J. Definition of Redox Centers in Reactions of Lithium Intercalation in Li3RuO4 Polymorphs. *Journal of the American Chemical Society* **2020**, *142* (18), 8160-8173. DOI: 10.1021/jacs.9b12438.
(11) Hong, J.; Gent, W. E.; Xiao, P.; Lim, K.; Seo, D. H.; Wu, J.; Csernica, P. M.; Takacs, C. J.; Nordlund, D.; Sun, C. J.; et al. Metal-oxygen decoordination stabilizes anion redox in Li-rich oxides. *Nature materials* **2019**, *18* (3), 256-265. DOI: 10.1038/s41563-018-0276-1.
(12) Pearce, P. E.; Perez, A. J.; Rousse, G.; Saubanère, M.; Batuk, D.; Foix, D.; McCalla, E.; Abakumov, A. M.; Van Tendeloo, G.; Doublet, M.-L.; et al. Evidence for anionic redox activity in a tridimensional-ordered Li-rich positive electrode β-Li2IrO3. *Nature materials* **2017**, *16* (5), 580-586. DOI: 10.1038/nmat4864.
(13) Perez, A. J.; Jacquet, Q.; Batuk, D.; Iadecola, A.; Saubanère, M.; Rousse, G.; Larcher, D.; Vezin, H.; Doublet, M.-L.; Tarascon, J.-M. Approaching the limits of cationic and anionic electrochemical activity with the Li-rich layered rocksalt Li3IrO4. *Nature Energy* **2017**, *2* (12), 954-962. DOI: 10.1038/s41560-017-0042-7.
(14) Li, H.; Taudul, B.; Alexander, G. C. B.; Liu, J.; Freeland, J. W.; Doublet, M.-L.; Cabana, J. Access to Ru(IV)–Ru(V) and Ru(V)–Ru(VI) Redox in Layered Li7RuO6 via Intercalation Reactions. *Chemistry of Materials* **2022**, *34* (8), 3724-3735. DOI: 10.1021/acs.chemmater.2c00043.
(15) Kubota, K.; Kaneko, T.; Hirayama, M.; Yonemura, M.; Imanari, Y.; Nakane, K.; Kanno, R. Direct synthesis of oxygen-deficient Li2MnO3−x for high capacity lithium battery electrodes. *Journal of Power Sources* **2012**, *216*, 249-255. DOI: https://doi.org/10.1016/j.jpowsour.2012.05.061.
(16) Armstrong, A. R.; Robertson, A. D.; Bruce, P. G. Overcharging manganese oxides: Extracting lithium beyond Mn4+. *Journal of Power Sources* **2005**, *146* (1), 275-280. DOI: https://doi.org/10.1016/j.jpowsour.2005.03.104.

(17) Francis Amalraj, S.; Markovsky, B.; Sharon, D.; Talianker, M.; Zinigrad, E.; Persky, R.; Haik, O.; Grinblat, J.; Lampert, J.; Schulz-Dobrick, M.; et al. Study of the electrochemical behavior of the “inactive” Li2MnO3. *Electrochimica Acta* **2012**, *78*, 32-39. DOI: https://doi.org/10.1016/j.electacta.2012.05.144.
(18) Rana, J.; Stan, M.; Kloepsch, R.; Li, J.; Schumacher, G.; Welter, E.; Zizak, I.; Banhart, J.; Winter, M. Structural Changes in Li2MnO3 Cathode Material for Li-Ion Batteries. *Advanced Energy Materials* **2014**, *4* (5), 1300998. DOI: 10.1002/aenm.201300998.
(19) Yan, P.; Xiao, L.; Zheng, J.; Zhou, Y.; He, Y.; Zu, X.; Mao, S. X.; Xiao, J.; Gao, F.; Zhang, J.-G.; et al. Probing the Degradation Mechanism of Li2MnO3 Cathode for Li-Ion Batteries. *Chemistry of Materials* **2015**, *27* (3), 975-982. DOI: 10.1021/cm504257m.
(20) House, R. A.; Rees, G. J.; Pérez-Osorio, M. A.; Marie, J.-J.; Boivin, E.; Robertson, A. W.; Nag, A.; Garcia-Fernandez, M.; Zhou, K.-J.; Bruce, P. G. First-cycle voltage hysteresis in Li-rich 3d cathodes associated with molecular O2 trapped in the bulk. *Nature Energy* **2020**, *5* (10), 777-785. DOI: 10.1038/s41560-020-00697-2.
(21) Chen, D.; Ahn, J.; Chen, G. An Overview of Cation-Disordered Lithium-Excess Rocksalt Cathodes. *ACS Energy Letters* **2021**, *6* (4), 1358-1376. DOI: 10.1021/acsenergylett.1c00203.
(22) Clément, R. J.; Lun, Z.; Ceder, G. Cation-disordered rocksalt transition metal oxides and oxyfluorides for high energy lithium-ion cathodes. *Energy & Environmental Science* **2020**, *13* (2), 345-373, 10.1039/C9EE02803J. DOI: 10.1039/C9EE02803J.
(23) Lun, Z.; Ouyang, B.; Kwon, D.-H.; Ha, Y.; Foley, E. E.; Huang, T.-Y.; Cai, Z.; Kim, H.; Balasubramanian, M.; Sun, Y.; et al. Cation-disordered rocksalt-type high-entropy cathodes for Li-ion batteries. *Nature materials* **2021**, *20* (2), 214-221. DOI: 10.1038/s41563-020-00816-0.
(24) Lee, J.; Kitchaev, D. A.; Kwon, D.-H.; Lee, C.-W.; Papp, J. K.; Liu, Y.-S.; Lun, Z.; Clément, R. J.; Shi, T.; McCloskey, B. D.; et al. Reversible Mn2+/Mn4+ double redox in lithium-excess cathode materials. *Nature* **2018**, *556* (7700), 185-190. DOI: 10.1038/s41586-018-0015-4.
(25) Yabuuchi, N.; Takeuchi, M.; Nakayama, M.; Shiiba, H.; Ogawa, M.; Nakayama, K.; Ohta, T.; Endo, D.; Ozaki, T.; Inamasu, T.; et al. High-capacity electrode materials for rechargeable lithium batteries: Li₃NbO₄-based system with cation-disordered rocksalt structure. *Proceedings of the National Academy of Sciences* **2015**, *112* (25), 7650-7655. DOI: 10.1073/pnas.1504901112.
(26) Lee, J.; Urban, A.; Li, X.; Su, D.; Hautier, G.; Ceder, G. Unlocking the Potential of Cation-Disordered Oxides for Rechargeable Lithium Batteries. *Science* **2014**, *343* (6170), 519-522. DOI: 10.1126/science.1246432.
(27) Freire, M.; Kosova, N. V.; Jordy, C.; Chateigner, D.; Lebedev, O. I.; Maignan, A.; Pralong, V. A new active Li-Mn-O compound for high energy density Li-ion batteries. *Nature materials* **2016**, *15* (2), 173-177. DOI: 10.1038/nmat4479.
(28) Yao, Z.; Kim, S.; He, J.; Hegde, V. I.; Wolverton, C. Interplay of cation and anion redox in Li₄Mn₂O₅ cathode material and prediction of improved Li₄(Mn,M)₂O₅ electrodes for Li-ion batteries. *Science Advances* **2018**, *4* (5), eaao6754. DOI: doi:10.1126/sciadv.aao6754.
(29) Freire, M.; Diaz-Lopez, M.; Bordet, P.; Colin, C. V.; Lebedev, O. I.; Kosova, N. V.; Jordy, C.; Chateigner, D.; Chuvilin, A. L.; Maignan, A.; et al. Investigation of the exceptional charge performance of the 0.93Li4−xMn2O5–0.07Li2O composite cathode for Li-ion batteries. *Journal of Materials Chemistry A* **2018**, *6* (12), 5156-5165, 10.1039/C8TA00234G. DOI: 10.1039/C8TA00234G.
(30) Diaz-Lopez, M.; Joly, Y.; Freire, M.; Colin, C.; Proux, O.; Pralong, V.; Bordet, P. Operando X-ray Absorption Spectroscopy and Emission Kβ1,3 Study of the Manganese Redox Activity in High-Capacity Li4Mn2O5 Cathode. *The Journal of Physical Chemistry C* **2018**, *122* (51), 29586-29597. DOI: 10.1021/acs.jpcc.8b09397.

(31) Toby, B. H.; Von Dreele, R. B. GSAS-II: the genesis of a modern open-source all purpose crystallography software package. *Journal of Applied Crystallography* **2013**, *46* (2), 544-549. DOI: 10.1107/s0021889813003531.
(32) Ravel, B.; Newville, M. ATHENA, ARTEMIS, HEPHAESTUS: data analysis for X-ray absorption spectroscopy using IFEFFIT. *Journal of Synchrotron Radiation* **2005**, *12* (4), 537-541. DOI: doi:10.1107/S0909049505012719.
(33) Yamamoto, T. Assignment of pre-edge peaks in K-edge x-ray absorption spectra of 3d transition metal compounds: electric dipole or quadrupole? *X-Ray Spectrometry* **2008**, *37* (6), 572-584. DOI: 10.1002/xrs.1103.
(34) Dau, H.; Liebisch, P.; Haumann, M. X-ray absorption spectroscopy to analyze nuclear geometry and electronic structure of biological metal centers—potential and questions examined with special focus on the tetra-nuclear manganese complex of oxygenic photosynthesis. *Analytical and Bioanalytical Chemistry* **2003**, *376* (5), 562-583. DOI: 10.1007/s00216-003-1982-2.
(35) Qiao, R.; Chin, T.; Harris, S. J.; Yan, S.; Yang, W. Spectroscopic fingerprints of valence and spin states in manganese oxides and fluorides. *Current Applied Physics* **2013**, *13* (3), 544-548. DOI: https://doi.org/10.1016/j.cap.2012.09.017.
(36) Groot, F. d.; Kotani, A. *Core Level Spectroscopy of Solids*; CRC Press, 2008.
(37) Shadle, S. E.; Hedman, B.; Hodgson, K. O.; Solomon, E. I. Ligand K-Edge X-ray Absorption Spectroscopy as a Probe of Ligand-Metal Bonding: Charge Donation and Covalency in Copper-Chloride Systems. *Inorganic Chemistry* **1994**, *33* (19), 4235-4244. DOI: 10.1021/ic00097a009.
(38) Wasinger, E. C.; de Groot, F. M. F.; Hedman, B.; Hodgson, K. O.; Solomon, E. I. L-edge X-ray Absorption Spectroscopy of Non-Heme Iron Sites: Experimental Determination of Differential Orbital Covalency. *Journal of the American Chemical Society* **2003**, *125* (42), 12894-12906. DOI: 10.1021/ja034634s.
(39) Risch, M.; Stoerzinger, K. A.; Han, B.; Regier, T. Z.; Peak, D.; Sayed, S. Y.; Wei, C.; Xu, Z.; Shao-Horn, Y. Redox Processes of Manganese Oxide in Catalyzing Oxygen Evolution and Reduction: An in Situ Soft X-ray Absorption Spectroscopy Study. *The Journal of Physical Chemistry C* **2017**, *121* (33), 17682-17692. DOI: 10.1021/acs.jpcc.7b05592.
(40) Laffont, L.; Gibot, P. High resolution electron energy loss spectroscopy of manganese oxides: Application to Mn3O4 nanoparticles. *Materials Characterization* **2010**, *61* (11), 1268-1273. DOI: https://doi.org/10.1016/j.matchar.2010.09.001.
(41) Qiao, R.; Chuang, Y. D.; Yan, S.; Yang, W. Soft x-ray irradiation effects of Li(2)O(2), Li(2)CO(3) and Li(2)O revealed by absorption spectroscopy. *PloS one* **2012**, *7* (11), e49182. DOI: 10.1371/journal.pone.0049182.
(42) Rana, J.; Papp, J. K.; Lebens-Higgins, Z.; Zuba, M.; Kaufman, L. A.; Goel, A.; Schmuch, R.; Winter, M.; Whittingham, M. S.; Yang, W.; et al. Quantifying the Capacity Contributions during Activation of Li2MnO3. *ACS Energy Letters* **2020**, *5* (2), 634-641. DOI: 10.1021/acsenergylett.9b02799.
(43) Xia, C.; Kwok, C. Y.; Nazar, L. F. A high-energy-density lithium-oxygen battery based on a reversible four-electron conversion to lithium oxide. *Science* **2018**, *361* (6404), 777-781. DOI: doi:10.1126/science.aas9343.
(44) Frati, F.; Hunault, M. O. J. Y.; de Groot, F. M. F. Oxygen K-edge X-ray Absorption Spectra. *Chemical Reviews* **2020**, *120* (9), 4056-4110. DOI: 10.1021/acs.chemrev.9b00439.

References (correct font)

(1) Zubi, G.; Dufo-López, R.; Carvalho, M.; Pasaoglu, G. The lithium-ion battery: State of the art and future perspectives. *Renew. Sust. Energ. Rev.* **2018**, *89*, 292-308. DOI: https://doi.org/10.1016/j.rser.2018.03.002.

(2) Trahey, L.; Brushett, F. R.; Balsara, N. P.; Ceder, G.; Cheng, L.; Chiang, Y.-M.; Hahn, N. T.; Ingram, B. J.; Minteer, S. D.; Moore, J. S.; et al. Energy storage emerging: A perspective from the Joint Center for Energy Storage Research. *Proc. Natl. Acad. Sci.* **2020**, *117* (23), 12550-12557. DOI: 10.1073/pnas.1821672117.

(3) Chen, T.; Jin, Y.; Lv, H.; Yang, A.; Liu, M.; Chen, B.; Xie, Y.; Chen, Q. Applications of Lithium-Ion Batteries in Grid-Scale Energy Storage Systems. *Trans. Tianjin Univ.* **2020**, *26* (3), 208-217. DOI: 10.1007/s12209-020-00236-w.

(4) Rozier, P.; Tarascon, J. M. Review—Li-Rich Layered Oxide Cathodes for Next-Generation Li-Ion Batteries: Chances and Challenges. *J. Electrochem. Soc.* **2015**, *162* (14), A2490-A2499. DOI: 10.1149/2.0111514jes.

(5) Thackeray, M. M.; Kang, S.-H.; Johnson, C. S.; Vaughey, J. T.; Benedek, R.; Hackney, S. A. Li_2MnO_3-stabilized $LiMO_2$ (M = Mn, Ni, Co) electrodes for lithium-ion batteries. *J. Mater. Chem.* **2007**, *17* (30), 3112. DOI: 10.1039/b702425h.

(6) Sathiya, M.; Rousse, G.; Ramesha, K.; Laisa, C. P.; Vezin, H.; Sougrati, M. T.; Doublet, M. L.; Foix, D.; Gonbeau, D.; Walker, W.; et al. Reversible anionic redox chemistry in high-capacity layered-oxide electrodes. *Nat. Mater.* **2013**, *12* (9), 827-835. DOI: 10.1038/nmat3699.

(7) He, W.; Guo, W.; Wu, H.; Lin, L.; Liu, Q.; Han, X.; Xie, Q.; Liu, P.; Zheng, H.; Wang, L.; et al. Challenges and Recent Advances in High Capacity Li-Rich Cathode Materials for High Energy

Density Lithium-Ion Batteries. *Adv. Mater.* **2021**, *33* (50), 2005937. DOI: https://doi.org/10.1002/adma.202005937.

(8) Gent, W. E.; Lim, K.; Liang, Y.; Li, Q.; Barnes, T.; Ahn, S. J.; Stone, K. H.; McIntire, M.; Hong, J.; Song, J. H.; et al. Coupling between oxygen redox and cation migration explains unusual electrochemistry in lithium-rich layered oxides. *Nat. Commun.* **2017**, *8* (1), 2091. DOI: 10.1038/s41467-017-02041-x.

(9) Jacquet, Q.; Perez, A.; Batuk, D.; Van Tendeloo, G.; Rousse, G.; Tarascon, J.-M. The $Li_3Ru_yNb_{1-y}O_4$ ($0 \leq y \leq 1$) System: Structural Diversity and Li Insertion and Extraction Capabilities. *Chem. Mater.* **2017**, *29* (12), 5331-5343. DOI: 10.1021/acs.chemmater.7b01511.

(10) Li, H.; Ramakrishnan, S.; Freeland, J. W.; McCloskey, B. D.; Cabana, J. Definition of Redox Centers in Reactions of Lithium Intercalation in Li_3RuO_4 Polymorphs. *J. Am. Chem. Soc.* **2020**, *142* (18), 8160-8173. DOI: 10.1021/jacs.9b12438.

(11) Hong, J.; Gent, W. E.; Xiao, P.; Lim, K.; Seo, D. H.; Wu, J.; Csernica, P. M.; Takacs, C. J.; Nordlund, D.; Sun, C. J.; et al. Metal-oxygen decoordination stabilizes anion redox in Li-rich oxides. *Nat. Mater.* **2019**, *18* (3), 256-265. DOI: 10.1038/s41563-018-0276-1.

(12) Pearce, P. E.; Perez, A. J.; Rousse, G.; Saubanère, M.; Batuk, D.; Foix, D.; McCalla, E.; Abakumov, A. M.; Van Tendeloo, G.; Doublet, M.-L.; et al. Evidence for anionic redox activity in a tridimensional-ordered Li-rich positive electrode β-Li_2IrO_3. *Nat. Mater.* **2017**, *16* (5), 580-586. DOI: 10.1038/nmat4864.

(13) Perez, A. J.; Jacquet, Q.; Batuk, D.; Iadecola, A.; Saubanère, M.; Rousse, G.; Larcher, D.; Vezin, H.; Doublet, M.-L.; Tarascon, J.-M. Approaching the limits of cationic and anionic electrochemical activity with the Li-rich layered rocksalt Li_3IrO_4. *Nat. Energy* **2017**, *2* (12), 954-962. DOI: 10.1038/s41560-017-0042-7.

(14) Li, H.; Taudul, B.; Alexander, G. C. B.; Liu, J.; Freeland, J. W.; Doublet, M.-L.; Cabana, J. Access to Ru(IV)–Ru(V) and Ru(V)–Ru(VI) Redox in Layered Li_7RuO_6 via Intercalation Reactions. *Chem. Mater.* 2022, 34 (8), 3724-3735. DOI: 10.1021/acs.chemmater.2c00043.

(15) Kubota, K.; Kaneko, T.; Hirayama, M.; Yonemura, M.; Imanari, Y.; Nakane, K.; Kanno, R. Direct synthesis of oxygen-deficient Li_2MnO_{3-x} for high capacity lithium battery electrodes. *J. Power Sources* **2012**, *216*, 249-255. DOI: https://doi.org/10.1016/j.jpowsour.2012.05.061.

(16) Armstrong, A. R.; Robertson, A. D.; Bruce, P. G. Overcharging manganese oxides: Extracting lithium beyond Mn^{4+}. *J. Power Sources* **2005**, *146* (1), 275-280. DOI: https://doi.org/10.1016/j.jpowsour.2005.03.104.

(17) Francis Amalraj, S.; Markovsky, B.; Sharon, D.; Talianker, M.; Zinigrad, E.; Persky, R.; Haik, O.; Grinblat, J.; Lampert, J.; Schulz-Dobrick, M.; et al. Study of the electrochemical behavior of the “inactive” Li_2MnO_3. *Electrochim. Acta* **2012**, *78*, 32-39. DOI: https://doi.org/10.1016/j.electacta.2012.05.144.

(18) Rana, J.; Stan, M.; Kloepsch, R.; Li, J.; Schumacher, G.; Welter, E.; Zizak, I.; Banhart, J.; Winter, M. Structural Changes in Li_2MnO_3 Cathode Material for Li-Ion Batteries. *Adv. Energy Mater.* **2014**, *4* (5), 1300998. DOI: https://doi.org/10.1002/aenm.201300998.

(19) Yan, P.; Xiao, L.; Zheng, J.; Zhou, Y.; He, Y.; Zu, X.; Mao, S. X.; Xiao, J.; Gao, F.; Zhang, J.-G.; et al. Probing the Degradation Mechanism of Li_2MnO_3 Cathode for Li-Ion Batteries. *Chem. Mater.* **2015**, *27* (3), 975-982. DOI: 10.1021/cm504257m.

(20) House, R. A.; Rees, G. J.; Pérez-Osorio, M. A.; Marie, J.-J.; Boivin, E.; Robertson, A. W.; Nag, A.; Garcia-Fernandez, M.; Zhou, K.-J.; Bruce, P. G. First-cycle voltage hysteresis in Li-rich 3d cathodes associated with molecular O_2 trapped in the bulk. *Nat. Energy* **2020**, *5* (10), 777-785. DOI: 10.1038/s41560-020-00697-2.

(21) Chen, D.; Ahn, J.; Chen, G. An Overview of Cation-Disordered Lithium-Excess Rocksalt Cathodes. *ACS Energy Lett.* **2021**, *6* (4), 1358-1376. DOI: 10.1021/acsenergylett.1c00203.

(22) Clément, R. J.; Lun, Z.; Ceder, G. Cation-disordered rocksalt transition metal oxides and oxyfluorides for high energy lithium-ion cathodes. *Energy Environ. Sci.* **2020**, *13* (2), 345-373, 10.1039/C9EE02803J. DOI: 10.1039/C9EE02803J.

(23) Lun, Z.; Ouyang, B.; Kwon, D.-H.; Ha, Y.; Foley, E. E.; Huang, T.-Y.; Cai, Z.; Kim, H.; Balasubramanian, M.; Sun, Y.; et al. Cation-disordered rocksalt-type high-entropy cathodes for Li-ion batteries. *Nat. Mater.* **2021**, *20* (2), 214-221. DOI: 10.1038/s41563-020-00816-0.

(24) Lee, J.; Kitchaev, D. A.; Kwon, D.-H.; Lee, C.-W.; Papp, J. K.; Liu, Y.-S.; Lun, Z.; Clément, R. J.; Shi, T.; McCloskey, B. D.; et al. Reversible Mn^{2+}/Mn^{4+} double redox in lithium-excess cathode materials. *Nature* **2018**, *556* (7700), 185-190. DOI: 10.1038/s41586-018-0015-4.

(25) Yabuuchi, N.; Takeuchi, M.; Nakayama, M.; Shiiba, H.; Ogawa, M.; Nakayama, K.; Ohta, T.; Endo, D.; Ozaki, T.; Inamasu, T.; et al. High-capacity electrode materials for rechargeable lithium batteries: Li_3NbO_4-based system with cation-disordered rocksalt structure. *Proc. Natl. Acad. Sci.* **2015**, *112* (25), 7650-7655. DOI: 10.1073/pnas.1504901112.

(26) Lee, J.; Urban, A.; Li, X.; Su, D.; Hautier, G.; Ceder, G. Unlocking the Potential of Cation-Disordered Oxides for Rechargeable Lithium Batteries. *Science* **2014**, *343* (6170), 519-522. DOI: 10.1126/science.1246432.

(27) Freire, M.; Kosova, N. V.; Jordy, C.; Chateigner, D.; Lebedev, O. I.; Maignan, A.; Pralong, V. A new active Li-Mn-O compound for high energy density Li-ion batteries. *Nat. Mater.* **2016**, *15* (2), 173-177. DOI: 10.1038/nmat4479.

(28) Yao, Z.; Kim, S.; He, J.; Hegde, V. I.; Wolverton, C. Interplay of cation and anion redox in $Li_4Mn_2O_5$ cathode material and prediction of improved $Li_4(Mn,M)_2O_5$ electrodes for Li-ion batteries. *Sci. Adv.* **2018**, *4* (5), eaao6754. DOI: doi:10.1126/sciadv.aao6754.

(29) Freire, M.; Diaz-Lopez, M.; Bordet, P.; Colin, C. V.; Lebedev, O. I.; Kosova, N. V.; Jordy, C.; Chateigner, D.; Chuvilin, A. L.; Maignan, A.; et al. Investigation of the exceptional charge performance of the $0.93Li_{4-x}Mn_2O_5$–$0.07Li_2O$ composite cathode for Li-ion batteries. *J. Mater. Chem. A* **2018**, *6* (12), 5156-5165, 10.1039/C8TA00234G. DOI: 10.1039/C8TA00234G.

(30) Diaz-Lopez, M.; Joly, Y.; Freire, M.; Colin, C.; Proux, O.; Pralong, V.; Bordet, P. Operando X-ray Absorption Spectroscopy and Emission $K\beta_{1,3}$ Study of the Manganese Redox Activity in High-Capacity $Li_4Mn_2O_5$ Cathode. *J. Phys. Chem. C* **2018**, *122* (51), 29586-29597. DOI: 10.1021/acs.jpcc.8b09397.

(31) Toby, B. H.; Von Dreele, R. B. GSAS-II: the genesis of a modern open-source all purpose crystallography software package. *J. Appl. Crystallogr.* **2013**, *46* (2), 544-549. DOI: 10.1107/s0021889813003531.

(32) Ravel, B.; Newville, M. ATHENA, ARTEMIS, HEPHAESTUS: data analysis for X-ray absorption spectroscopy using IFEFFIT. *J. Synchrotron Radiat.* **2005**, *12* (4), 537-541. DOI: doi:10.1107/S0909049505012719.

(33) Yamamoto, T. Assignment of pre-edge peaks in K-edge x-ray absorption spectra of 3d transition metal compounds: electric dipole or quadrupole? *X-Ray Spectrometry* **2008**, *37* (6), 572-584. DOI: 10.1002/xrs.1103.

(34) Dau, H.; Liebisch, P.; Haumann, M. X-ray absorption spectroscopy to analyze nuclear geometry and electronic structure of biological metal centers—potential and questions examined

with special focus on the tetra-nuclear manganese complex of oxygenic photosynthesis. *Anal. Bioanal. Chem.* **2003**, *376* (5), 562-583. DOI: 10.1007/s00216-003-1982-2.

(35) Qiao, R.; Chin, T.; Harris, S. J.; Yan, S.; Yang, W. Spectroscopic fingerprints of valence and spin states in manganese oxides and fluorides. *Curr. Appl Phys.* **2013**, *13* (3), 544-548. DOI: https://doi.org/10.1016/j.cap.2012.09.017.

(36) Groot, F. d.; Kotani, A. *Core Level Spectroscopy of Solids*; CRC Press, 2008.

(37) Shadle, S. E.; Hedman, B.; Hodgson, K. O.; Solomon, E. I. Ligand K-Edge X-ray Absorption Spectroscopy as a Probe of Ligand-Metal Bonding: Charge Donation and Covalency in Copper-Chloride Systems. *Inorg. Chem.* **1994**, *33* (19), 4235-4244. DOI: 10.1021/ic00097a009.

(38) Wasinger, E. C.; de Groot, F. M. F.; Hedman, B.; Hodgson, K. O.; Solomon, E. I. L-edge X-ray Absorption Spectroscopy of Non-Heme Iron Sites: Experimental Determination of Differential Orbital Covalency. *J. Am. Chem. Soc.* **2003**, *125* (42), 12894-12906. DOI: 10.1021/ja034634s.

(39) Risch, M.; Stoerzinger, K. A.; Han, B.; Regier, T. Z.; Peak, D.; Sayed, S. Y.; Wei, C.; Xu, Z.; Shao-Horn, Y. Redox Processes of Manganese Oxide in Catalyzing Oxygen Evolution and Reduction: An *in Situ* Soft X-ray Absorption Spectroscopy Study. *J. Phys. Chem. C* **2017**, *121* (33), 17682-17692. DOI: 10.1021/acs.jpcc.7b05592.

(40) Laffont, L.; Gibot, P. High resolution electron energy loss spectroscopy of manganese oxides: Application to Mn_3O_4 nanoparticles. *Mater. Charact.* **2010**, *61* (11), 1268-1273. DOI: https://doi.org/10.1016/j.matchar.2010.09.001.

(41) Qiao, R.; Chuang, Y. D.; Yan, S.; Yang, W. Soft x-ray irradiation effects of Li_2O_2, Li_2CO_3 and Li_2O revealed by absorption spectroscopy. *PloS one* **2012**, *7* (11), e49182. DOI: 10.1371/journal.pone.0049182.

(42) Rana, J.; Papp, J. K.; Lebens-Higgins, Z.; Zuba, M.; Kaufman, L. A.; Goel, A.; Schmuch, R.; Winter, M.; Whittingham, M. S.; Yang, W.; et al. Quantifying the Capacity Contributions during Activation of Li_2MnO_3. *ACS Energy Lett.* **2020**, *5* (2), 634-641. DOI: 10.1021/acsenergylett.9b02799.

(43) Xia, C.; Kwok, C. Y.; Nazar, L. F. A high-energy-density lithium-oxygen battery based on a reversible four-electron conversion to lithium oxide. *Science* **2018**, *361* (6404), 777-781. DOI: doi:10.1126/science.aas9343.

(44) Frati, F.; Hunault, M. O. J. Y.; de Groot, F. M. F. Oxygen K-edge X-ray Absorption Spectra. *Chem. Rev.* **2020**, *120* (9), 4056-4110. DOI: 10.1021/acs.chemrev.9b00439.

TOC Graphic